

Generation of MeV electrons and positrons with femtosecond pulses from a table-top laser system

C. Gahn, G. D. Tsakiris,^{a)} G. Pretzler, and K. J. Witte
Max-Planck-Institut für Quantenoptik, D-85748 Garching, Germany

P. Thirolf and D. Habs
Sektion Physik, LMU München, Am Coulombwall 1, D-85748 Garching, Germany

C. Delfin and C.-G. Wahlström
Department of Physics, Lund Institute of Technology, P.O. Box 118, S-221 00 Lund, Sweden

(Received 29 August 2001; accepted 4 December 2001)

In experiments, the feasibility was demonstrated of generating multi-MeV electrons in a form of a collimated beam utilizing a table-top laser system delivering 200 fs pulses with $P_L = 1.2$ TW and 10 Hz capability. The method uses the process of relativistic self-channeling in a high-density gas jet producing electron densities in the range of $3 \times 10^{19} - 6 \times 10^{20} \text{ cm}^{-3}$. In a thorough investigation, angularly resolved and absolutely calibrated electron spectra were measured and their dependence on the plasma density, laser intensity, and gas medium was studied. For the optimum electron density of $n_e = 2 \times 10^{20} \text{ cm}^{-3}$ the effective temperature of the electron energy distribution and the channel length exhibit a maximum of 5 MeV and 400 μm respectively. The laser-energy-to-MeV-electron efficiency is estimated to be 5%. In a second step, utilizing the multi-MeV electron beam anti-particles, namely positrons, were successfully generated in a 2 mm Pb converter. The average intensity of this new source of positrons is estimated to be equivalent to a radioactivity of 2×10^8 Bq and it exhibits a very favorable scaling for higher laser intensities. © 2002 American Institute of Physics. [DOI: 10.1063/1.1446879]

I. INTRODUCTION

Present-day high-repetition-rate table-top laser systems deliver focused intensities approaching 10^{20} W/cm^2 while large-scale petawatt class lasers pledge intensities beyond 10^{21} W/cm^2 for the foreseeable future. These technological advances in the development of multi-terawatt short pulse lasers have spurred research activities in a new intensity regime of laser matter interaction identified as high-intensity physics.¹ Appealingly, a number of experiments in this vigorously pursued new area of physics indicate that moderate size table-top laser systems could conceivably replace the large accelerator facilities for a number of applications. Indeed, using 10 Hz, TW table-top lasers the generation of MeV γ -rays in the interaction of solid targets with femtosecond-laser pulses has been reported.^{2,3} Generation of XUV radiation in form of harmonics of the fundamental has also been demonstrated.⁴⁻⁶ Furthermore, fusion neutrons using either deuterated planar targets⁷ or deuterium clusters⁸ heated with femtosecond laser pulses have been observed. More recently, 10^{10} electrons per laser pulse were produced in a low emittance beam with average energies of 5 MeV and maximum extending to over 12 MeV.⁹ In a miniaturized scheme analogous to the one utilized in linear accelerators, these MeV laser accelerated electrons were used to generate anti-particles, namely positrons.¹⁰

Independently, the propagation of ultrashort high-intensity laser pulses through fully ionized plasma and the

accompanied process of electron acceleration is of particular interest for three main reasons: (a) It is intimately connected to the physics of the plasma based accelerators that can sustain extremely large acceleration gradients of the order of $\sim 1 \text{ GV/cm}$. Because this is four orders of magnitude higher than in conventional accelerators, they hold out the promise to replace the large scale rf linacs with more compact devices.¹¹ (b) In the advanced inertial confinement fusion scheme known as “fast ignitor,” the laser accelerated electrons play an important role in transporting the energy through an overdense plasma to the fuel.¹² (c) Laser based production of nuclear radiation (γ -rays, neutrons, positrons, pions) or laser induced nuclear reactions require large fluxes of relativistic electrons.^{13,14}

In this report we give a comprehensive account of the work we have performed on the generation of a relativistic electron beam employing a table-top laser system delivering femtosecond pulses at the rate of 10 Hz. Also, of an application in which, using the laser accelerated electrons, we produced 10^6 positrons (e^+) per laser pulse with a mean energy of ~ 2 MeV. The measured electron energy spectra, resolved in angle and absolutely calibrated, pertain to electron acceleration during self-channeling in a previously unexplored regime, characterized by fs-laser pulses of relatively low energy ($< 1 \text{ J}$) interacting with a high-density gas jet producing electron densities $n_e \sim 0.3n_c$ where $n_c = m\omega_L^2/(4\pi e^2)$ is the plasma critical density corresponding to the laser frequency ω_L . A brief account of this work has already been communicated in Refs. 9 and 10. Even though the generation of relativistic electrons with short laser pulses

^{a)}Electronic mail: tsakiris@mpq.mpg.de

in gas-jet targets has been reported in a number of similar investigations,^{15–18} to our knowledge this is the first experiment in which an 1-TW table-top laser system operating at 10 Hz was utilized for that purpose. Recently, similar measurements were reported using the same type of laser but at higher intensities.¹⁹ In this context, our work represents a further development toward a particle source of table-top size. When operating at 10 Hz, radiation safety rules concerning the personnel performing the experiment require careful shielding of the area around the gas-jet target in order to reduce the radiation dosage to acceptable level. This makes the experimental setup inflexible and the experimentation cumbersome. To avoid this complication, we have chosen to perform the measurements using single laser pulses. It should be stressed here though that there are no technical constraints hindering the operation of the source at the laser repetition rate, i.e., 10 Hz. Under these circumstances, this experiment demonstrates the realization of a switchable e^+ source with an equivalent activity of 2×10^8 Bq.

After an epigrammatic review of the interaction physics of TW laser pulses with gas-jet targets and of the electron acceleration mechanisms in Sec. II, we present the experimental setup along with the main experimental results from the fast electron generation in Sec. III. The application of positron generation and detection is described in Sec. IV. The conclusions and some potential prospects are given in Sec. V.

II. HIGH-INTENSITY LASER PULSE INTERACTION WITH UNDERDENSE PLASMA

A. Self-focusing and channel formation

The first phase of the interaction of a high-intensity pulse with neutral gas is the rapid medium ionization by its leading edge so that the subsequent interaction is that of an intense pulse with an underdense plasma. A Gaussian-like radial intensity profile would produce via ionization an excess of electrons around the beam axis, which would lead to defocusing because of the lensing effect associated with such a density profile. In addition, the diffraction of the beam leads to defocusing independently of density or intensity. A counteracting process is the relativistically induced self-focusing due to the electron mass increase in high-intensity regions followed by the ponderomotive self-focusing as a result of the expulsion of electrons from the region around the propagation axis.

In the limit where the laser pulse contains many laser oscillations, the refractive index of the plasma η is given by^{20–23}

$$\eta \approx 1 - \frac{1}{2} \frac{\omega_p^2}{\gamma \omega_L^2}, \quad (1)$$

where $\omega_p = (4\pi e^2 n_e / m)^{1/2}$ is the plasma frequency, n_e the electron density, and ω_L the laser frequency. The factor γ in Eq. (1) is due to relativistic mass increase of the electron executing a quiver motion in the laser field and in terms of the normalized vector potential $a_L = eE_L / mc\omega_L$ is given by $\gamma = (1 + a_L^2/2)^{1/2}$ with E_L the peak electric field. For low (nonrelativistic) intensities $a_L^2 \approx 0$ thus its effect diminishes.

Given that $\omega_p^2 \sim n_e$, one sees that the ionization of the medium at the high-intensity region results in a decrease of the index of refraction, but at the same time the higher value of a_L counteracts this increase via the factor γ with a decrease. In the case of high intensities and low Z gases, the medium ionizes completely so that the pulse propagates through a homogeneous plasma of constant electron density. Under these circumstances, there are no contributions from the ionization defocusing term in Eq. (1) and the relativistic self-focusing has to compete with diffraction only.²⁴ For the relativistic self-focusing to dominate over diffraction the well known condition $P_L > P_c$ has to be fulfilled with P_L the laser beam power and $P_c \approx 16.4(\omega_L^2 / \omega_p^2)$ GW the critical power for a given electron density and laser frequency.^{20,25–28} The ponderomotive contribution to self-focusing is generally stronger than the relativistic but not instantaneous. This is because it is associated with charge displacement which involves an inertial response.

Theoretical analysis has shown that depending on the initial laser and plasma conditions, the intense short-pulse undergoes relativistic self-focusing can propagate either in a stable single channel mode or can break up in filaments thus exhibiting unstable behavior.²⁹ Recently, the transition from whole beam focusing to strong filamentation regime has been observed.³⁰ More insight in the process of filamentation has been gained by three-dimensional Particle-In-Cell (PIC) simulations.³¹ It is believed that the filamentation is seeded by the Weibel instability occurring in the flow of energetic electrons produced by, e.g., stimulated Raman scattering and propagating in the laser direction. The current filamentation is accompanied by light filamentation and strong quasi-static magnetic fields. However, the three-dimensional PIC simulations have revealed a new phenomenon in which after the beam passes through an unstable filamentary phase it shrinks into a single channel having a diameter of a few wavelengths.³¹ The coalescence of the light and current filaments into a single channel for $a_L > 1$ is attributed to the mutual attraction of nearby located current filaments and it is accompanied by a factor > 10 enhancement of the on-axis light intensity. The plasma channel acts as a dielectric light guiding waveguide which can transport the high-intensity pulse over considerable distances. This effect of relativistic self-channeling leading to the formation of a single channel has been observed experimentally.³²

B. Electron acceleration

Concomitant to the self-focusing is the generation of relativistic electrons with energies of several tens of MeVs. These energies greatly exceed the maximum kinetic energy $a_L^2 mc^2/2$ acquired by a single electron in the focused laser beam, which for $a_L \approx 1$ would be 250 keV only. Obviously, collective effects associated with the plasma through which the laser plasma propagates are responsible for the observed relativistic electron energies. Two mechanisms are currently under scrutiny: The Laser Wakefield Acceleration (LWFA) and the Direct Laser Acceleration (DLA).

In the LWFA, a short laser pulse excites an electron plasma wave by expelling the electrons from the space that it

occupies. This is due to the ponderomotive force associated with the pulse envelope and it is optimally driven when the pulse length $L = c\tau_L$ matches half the plasma wavelength $\lambda_p/2 = \pi c/\omega_p$.^{11,23} This process combined with the restoring force due to ion inertia leads to the creation of a longitudinal electrostatic wake field propagating with a phase velocity equal to the group velocity of the laser pulse in the plasma. Background electrons are trapped in the potential well of such a wave and they are accelerated in the direction of propagation. When the amplitude of the electron oscillations in the plasma well becomes comparable with the plasma wavelength, wave-breaking occurs in which the plasma wave loses its coherent nature. The trapped electrons damp the wave irreversibly and appear as a collimated relativistic electron beam.^{16,33,34} The maximum energy to which the self-trapped electron can be accelerated depends primarily on two factors. First, on the maximum possible acceleration gradient before wave-breaking occurs and second, on the phase slippage between electron plasma wave and accelerated particles. The last factor is referred to as “dephasing limit” and it corresponds to the case where the electron has acquired so much energy that it moves ahead of the accelerating flank of the potential well and starts de-accelerating.¹⁷ The maximum electron energy gain through this process has been shown to be $\gamma_{\max} = 2\omega^2/\omega_p^2$,³⁵ which indicates that lower plasma densities favor high energy gain, but this presumes long acceleration lengths which is difficult to produce in practice. In the high density regime in which the laser pulse duration encompasses several plasma periods, i.e., $\tau_L > 2\pi/\omega_p$, the laser envelope undergoes an instability and becomes “self-modulated” at the plasma period.³⁶ The pulse breaks up into multiple pulses each having the optimum length and thus it resonantly drives large-amplitude plasma waves. The associated process of electron acceleration in the wake field thus created is referred to as Self-Modulated Laser Wakefield Acceleration (SM-LWFA).

The second mechanism of Direct Laser Acceleration³⁷ presumes the existence of strong quasi-static fields inherent to the formation of the channel. A part of the initial electron population occupying the channel volume is displaced because of the radial ponderomotive force exerted by the laser pulse. As a result of the charge separation, a strong radial electric field is generated. Another part of the initial number of electrons is pre-accelerated in the axial direction by the excitation of a plasma wave in the leading edge of the laser pulse via the forward Raman instability. These energetic electrons carry an electric current which produces an azimuthal magnetic field. A relativistic electron moving in the combined radial electric and azimuthal magnetic field executes a motion which is similar to the one in a wiggler field of a free electron laser.³⁸ It oscillates in the transverse direction at the betatron frequency $\omega_b \approx \omega_p/(2\gamma)^{1/2}$ in these fields while drifting along the channel together with the laser pulse. When the frequency of betatron oscillations coincides with the Doppler shifted laser frequency, as seen by the relativistic electron, a resonance occurs, leading to an effective energy exchange between the laser and the electron. As described in Ref. 37, this mechanism is similar to that of inverse free electron lasers (IFEL),³⁹ with the wiggler field replaced by

the self-generated quasi-static electric and magnetic fields in the channel.^{31,40}

It should be noted here that no delimitation for the validity of the two mechanisms in the pertinent parameter space (laser intensity, plasma density, pulse duration, focusing geometry) is available. However, three-dimensional PIC code simulations indicate that for high plasma densities and relatively long laser pulses where the condition $\tau_L > \pi/\omega_p$ is satisfied, the DLA is most likely the dominant mechanism. On the other hand, for short laser pulses and low plasma densities the LWFA appears to be the main acceleration mechanism.

III. GENERATION AND CHARACTERIZATION OF THE RELATIVISTIC ELECTRON BEAM

A. The experimental setup

The experiment was performed with the first module of the 10 Hz advanced Ti:sapphire laser ATLAS at Max-Planck-Institut für Quantenoptik that delivers pulses at 790 nm as short as 130 fs and with a maximum energy of 250 mJ. The whole laser chain consisting of the oscillator, stretcher, two amplification stages (regenerative plus multi-pass amplifier), and compressor is assembled on two optical tables. To avoid deterioration of the high-intensity pulse, the beam after compression is transported to the experimental chamber in vacuum. The main experimental setup is shown in the perspective view of Fig. 1.

The laser beam was focused with an $F_{\#} = 3$ high-quality off-axis parabolic mirror, which ensures high focal intensities. The radial beam profile at focus was measured using the equivalent focal plane technique in which a high resolution multiple element objective with $F_{\#} = 2.5$ and $f = 10$ cm is employed to image the focal spot plane into a charge-coupled device (CCD) camera with a magnification factor of ~ 50 and a spatial resolution of $\sim 1 \mu\text{m}$. The overall dynamic range of the CCD camera was extended using several ND filters and numerically combining records taken under different exposure conditions. The thus obtained radial beam profile was numerically integrated to obtain the azimuthally averaged power within a radius r , i.e., $P(r) = \int_0^r \int_0^{2\pi} I(\rho, \phi) \rho d\rho d\phi$. The result is given in Fig. 2. One immediate observation is that 86% of the beam energy is confined in a spot size having a radius of $\approx 7.5 \mu\text{m}$. The azimuthally averaged radial intensity distribution is approximately obtained by fitting a double Gaussian of the form $P(r) = P_L [A(1 - e^{-2(r/r_a)^2}) + (1 - A)(1 - e^{-2(r/r_b)^2})]$ to the experimental data for the power. This corresponds to a double Gaussian intensity profile of the form: $I(r) = I_a + I_b = P_L [(2A/\pi r_a^2) e^{-2(r/r_a)^2} + (2(1 - A)/\pi r_b^2) e^{-2(r/r_b)^2}]$.

The relative amplitude of the two Gaussian profiles A and their $1/e^2$ intensity radii r_a, r_b are the free parameters used for the fitting. The fitted power $P(r)$ and the corresponding intensity distribution $I(r)$ are included in Fig. 2. As it can be seen, the focal spot profile consists of a narrower peak with a $1/e^2$ intensity radius of $r_a = 3.0 \mu\text{m}$ superimposed on a low level broad background with radius of $r_b = 10.0 \mu\text{m}$. Furthermore, for $A = 0.46$ the relative contribution to the peak intensity of the two Gaussians is 9:1 result-

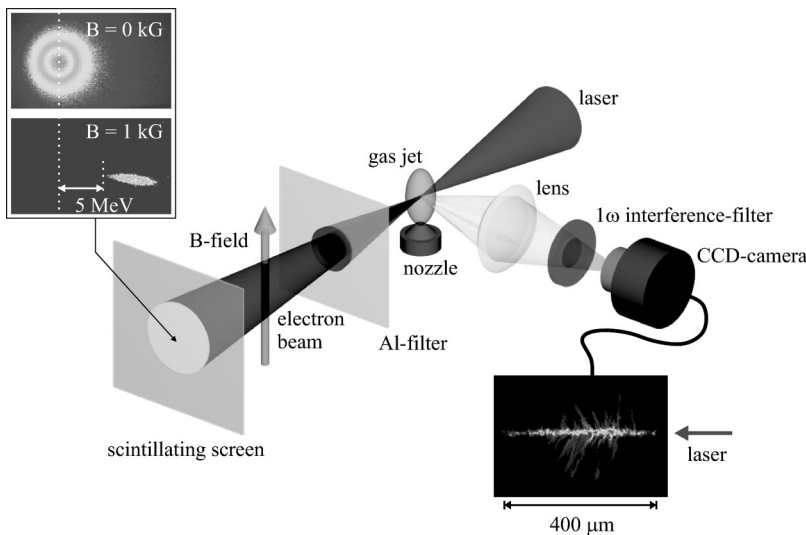


FIG. 1. Schematic of the experimental arrangement showing two of the diagnostics used. The side view CCD camera for the self-scattered image with which the channel formation was established and its length measured (lower right insert) and the scintillating screen used for the visualization and optimization of the generated electron. The appearance of MeV electrons is demonstrated by utilizing a magnetic field that deflects the electron according to their energy (top left insert).

ing in a combined peak intensity at focus of $I(0) \sim 4.5 \times 10^{18} \text{ W/cm}^2$. The data presented here were acquired over a number of experimental series during which the peak intensity fluctuated between $4.0 \times 10^{18} \text{ W/cm}^2$ and $6.5 \times 10^{18} \text{ W/cm}^2$ mainly due to replacement of optical components in the laser system. This results in a normalized vector potential range of $a_L \sim 1.4\text{--}1.7$. Of importance here is the confocal parameter defined for a single Gaussian beam as twice the Rayleigh length $2z_0 = 2\pi r_0^2/\lambda$ with r_0 the $1/e^2$ intensity radius. The high-intensity Gaussian peak is responsible for the self-focusing and channeling of the laser beam and hence, it is reasonable to compare the channel length to the confocal parameter $2z_0 \approx 70 \mu\text{m}$ corresponding to its $1/e^2$ intensity radius $r_0 = r_a \approx 3.0 \mu\text{m}$. The observed axial profile of the vacuum focus confirms this estimate (see Fig. 4 below). As discussed in Ref. 24, the focal spot profile plays a decisive role on the beam interaction processes with a gas jet. In the early stages of the interaction when refractive defocusing is important, the double Gaussian profile might be of advantage as it provides an environment of fully ionized plasma through which the high-intensity peak propagates.

The focus was placed at the edge of a free expansion gas jet generated by a high pressure gas nozzle with a circular

orifice of $500 \mu\text{m}$ in diameter.^{24,41} The gas density profile was measured interferometrically for the different gases used in the present experiment including, hydrogen, argon and nitrogen. The density profiles at a distance of $100\text{--}400 \mu\text{m}$ from the nozzle outlet can be adequately characterized by a simple Gaussian radial profile and an exponential density fall off with distance from the nozzle orifice. The accuracy of the density measurements was estimated to be $\pm 25\%$. As shown in Fig. 3, the radial (along the laser direction) density profile in the interaction region located $\sim 100 \mu\text{m}$ above the nozzle tip corresponds to a Gaussian profile with half the peak density at the edge of the orifice. The peak molecular density at this position is linearly proportional to the backing pressure up to a maximum value of $3 \times 10^{20} \text{ cm}^{-3}$ (see Fig. 3). Most of the measurements reported here were made using helium producing electron densities in the range $n_e/n_c \approx 0.05\text{--}0.3$.

In order to diagnose self-focusing and channel formation, a side-scattering imaging system at 90° to the laser beam direction was utilized (see Fig. 1). Using an interference filter this system took self-scattered time integrated images of the radiation at the fundamental laser wavelength

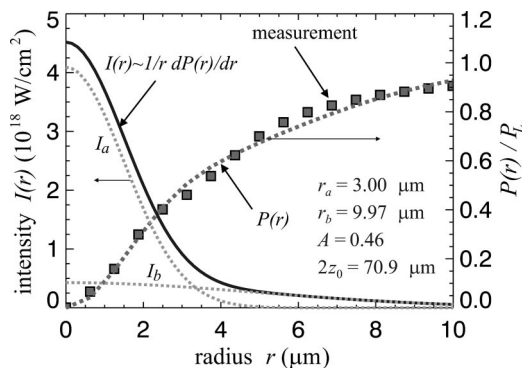


FIG. 2. Radial beam profile at focus. Squares: measured radial power distribution. Dashed line: double Gaussian fit. Solid line: The total focal intensity distribution resulting from the sum of the two Gaussian profiles I_a and I_b (thin dotted lines).

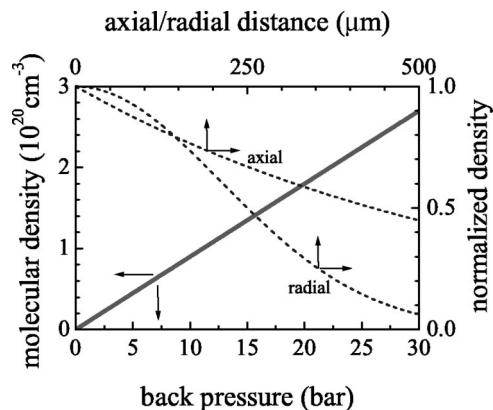


FIG. 3. Interferometrically measured molecular density dependence on the nozzle back pressure (solid line). The normalized axial and radial density profile at a distance of $\sim 100 \mu\text{m}$ above the nozzle orifice are also shown (dotted lines).

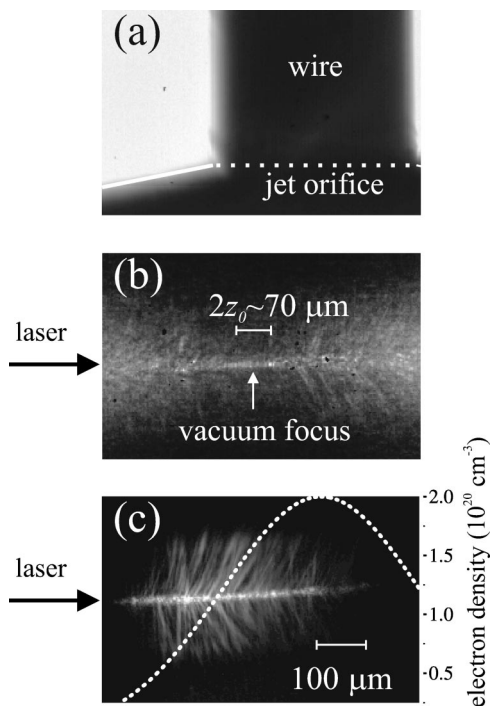


FIG. 4. Side view image of the channel due to self-scattering. (a) Jet orifice with a 400 μm wire inserted in its opening. (b) Vacuum focus obtained in a static filled chamber with 10 mbar nitrogen. (c) Image of the channel indicating its position relative to the gas density profile (dotted line).

with a spatial resolution of 5 μm. The same setup was also used to precisely position the vacuum focus of the laser beam relative to the gas plume emanating from the nozzle orifice. First, by static fill of the experimental chamber with 10 mbar nitrogen the vacuum focus was localized. This is shown in Fig. 4(b) where also the confocal parameter of the focusing optics is seen to be in good agreement with the estimate obtained from the focal spot size (see Fig. 2). The position of the nozzle orifice and the exact magnification of the setup was obtained by back-lighting a 400 μm diameter wire inserted in the opening of the nozzle [Fig. 4(a)]. This way the position of the vacuum focus could be varied in the laser beam direction relative to the peak of the density profile. It was found experimentally that the longest channels are formed when the vacuum focus is at the position where the density is about half maximum independently of peak density value. This is depicted in Fig. 4(c) where a ~400 μm long channel is shown relative to the radial density profile.

Two different diagnostics for electron detection were employed. The first one is shown schematically in Fig. 1 and consists of a phosphorescent screen placed behind a 100-μm-thick aluminum foil that blocked the laser light and electrons with energies less than 200 keV. The purpose of this device was to visualize the relativistic electrons and qualitatively optimize their production. At an electron density of $3 \times 10^{19} \text{ cm}^{-3}$ a faint round spot appeared on the screen centered on the laser axis and it became brighter at higher densities. When a static magnetic field of 1 kG was applied between the filter and the screen, this spot moved in the direction expected for a beam of electrons (see Fig. 1). A

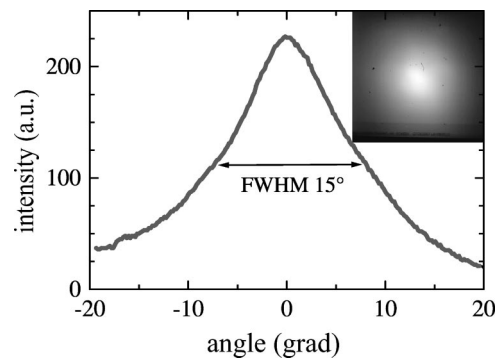


FIG. 5. Radial electron beam profile as obtained from a line-out of the spot image (inset) on the phosphorescent screen for $n_e = 1.3 \times 10^{20} \text{ cm}^{-3}$. The image includes all electron energies above 200 KeV.

line-out of the electron spot on the phosphorescent screen is given in Fig. 5. This gives an approximate estimate of the overall electron beam divergence as ~15° FWHM (full width at half maximum). This is an upper limit because the low energy electrons suffer multi-Coulomb scattering in the aluminum foil and thus increase the size of the spot.

The main electron diagnostic was a compact 45-channel magnetic spectrometer,⁴² which after beam optimization replaced the filter and screen and with which quantitative measurements of the electron energy distribution in a range from 500 keV up to 12.5 MeV were performed. Figure 6 illustrates the setup for the electron spectrum measurements. The electrons were collimated by an aperture of 5 mm in diameter, dispersed by a permanent dipole magnet and finally detected by scintillating/light-guiding plastic fibers which were coupled via a fiber optics to a cooled CCD camera. Subsequently, from the recorded image of the fiber array the energy spectrum was deduced. The aperture was located 14 cm away from the laser focus resulting in 1 msr collection angle for the spectrometer.

The spectrometer was absolutely calibrated using various β-emitters. The detailed description and operational characteristics of this novel spectrometer are given in Ref. 42. The compact size of the spectrometer and its flexible connection via the plastic fiber bundle to the detector made possible the rotation of the whole permanent magnet unit horizontally as well as vertically around the interaction region up to an angle of 10° relative to the laser beam direction. A schematic of this arrangement is shown in Fig. 7. This

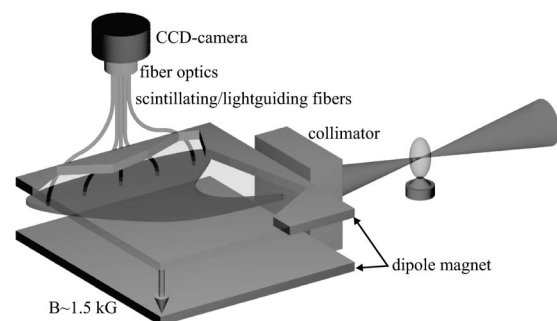


FIG. 6. Schematic showing the 45-channel electron spectrometer using scintillating fibers (see Ref. 42).

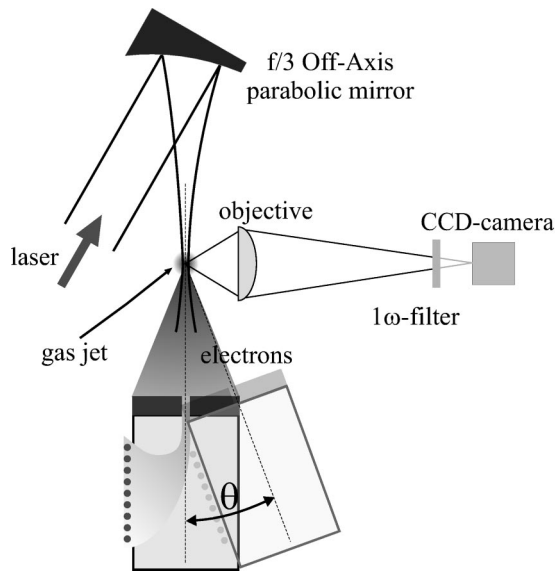


FIG. 7. Schematic diagram illustrating the method used to measure the angular dependence of the electron spectrum. The spectrometer was pivoted around the gas jet in steps of 2.5°.

way measurement of the angular dependence of the electron energy distribution was made feasible.

B. Experimental results

1. Electron energy distribution

A typical energy spectrum that was measured in the laser beam direction (from now on denoted by 0°) at the maximum laser intensity (see Fig. 2) and at an electron density of $2 \times 10^{20} \text{ cm}^{-3}$ is shown in Fig. 8. As has already been established in experiments with longer laser pulses,^{16–18} the high energy electrons ($E > 1 \text{ MeV}$), exhibit a Boltzmann-like distribution $N(E) = N_0 e^{-E/T_{\text{eff}}}$ with an effective temperature of $T_{\text{eff}} = 5 \text{ MeV}$. The maximum energy detected is 12.5 MeV, which was the spectrometer limit. It should be pointed out here that the sensitivity of the electron detector allows the acquisition of this spectrum in a single laser pulse. It was found that for the same set of parameters the energy spectrum is very reproducible. Thus, as seen from Fig. 8, about 10^8 electrons per msr with mean kinetic energy of 5 MeV

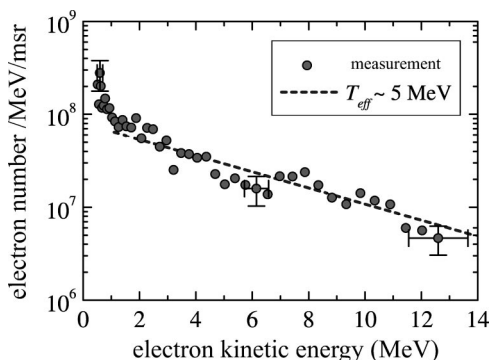


FIG. 8. Typical electron spectrum measured in laser beam direction (circles) and exponential fit (dotted line) for the optimum electron density $n_e = 2 \times 10^{20} \text{ cm}^{-3}$.

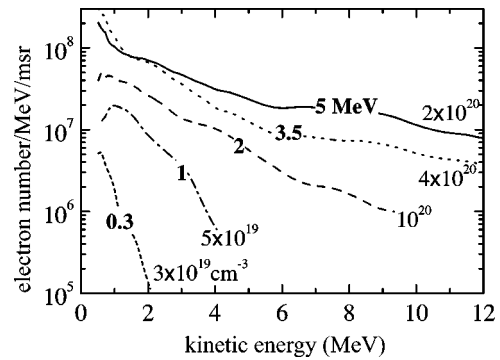


FIG. 9. Experimentally determined electron-spectrum dependence on different electron densities (labeled by normal letters). Bold letters give the effective temperatures of the (not shown) exponential fits.

can be readily generated at the rate of 10 Hz. In what follows the results of the experimental investigation of the electron energy distribution dependence on density, angle, laser intensity and gas medium are outlined.

2. Electron density dependence

For a given laser power and frequency, the threshold for relativistic self-focusing $P_{\text{RSF}} = P_c \approx 16.4 (\omega_L^2 / \omega_p^2) \text{ GW}$ can be traversed by lowering the critical power via density variation. The onset of self-focusing can be observed experimentally this way and it is depicted in Figs. 9 and 10 where the parallel evolution of the channel length and that of the effective electron temperature is given. As seen from Fig. 10, at an electron density of $3 \times 10^{19} \text{ cm}^{-3}$, i.e., slightly above the threshold for self-focusing the channel length starts to become longer than the confocal parameter (twice the Rayleigh length $2z_0 \approx 70 \mu\text{m}$) and the first relativistic electrons appear (see Fig. 9). When the density is increased to $5 \times 10^{19} \text{ cm}^{-3}$, a self-focused channel of $220 \mu\text{m}$ is observed and the temperature of the fast electrons measured at 0° rises strikingly from 300 keV to 1 MeV (see Fig. 9). This tendency continues under further density increase until a density of $2 \times 10^{20} \text{ cm}^{-3}$ where the maximum temperature of 5.0 MeV and the longest channel of $\sim 400 \mu\text{m}$ are detected. Simultaneously, an increase in the total number of MeV-electrons is perceived reaching a value of $3.3 \times 10^8 / \text{msr}$

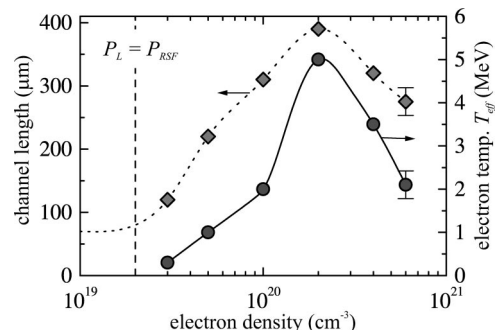


FIG. 10. Dependence of channel length (diamonds) and effective electron temperature (circles) on plasma density. Symbols correspond to the experimental data while the solid and dotted line are to guide the eye. The vertical dashed line shows the theoretical threshold for relativistic self-focusing.

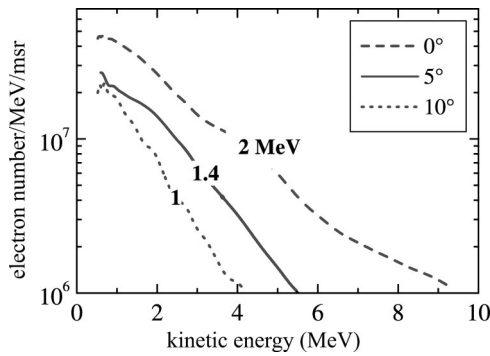


FIG. 11. Measured electron energy distribution within the solid angle of $\Delta\Omega = 1$ msr for the in the inset indicated angles relative to the laser axis and for $n_e = 10^{20} \text{ cm}^{-3}$. The effective temperature corresponding to each distribution is noted on the curve.

optimum density (see Sec. III B 3). As can be seen from Fig. 10, additional increase in density reverses this trend and results in a drop of the effective temperature and channel length.

As the plasma density increases, the self-focusing power threshold drops, and the effective ratio P_L/P_c rises. A larger portion of the laser beam is trapped in the channel and its length grows. At the plasma density of $n_e = 2 \times 10^{20} \text{ cm}^{-3}$ we observe an optimum at which most of the laser energy is trapped in the channel (Fig. 10). Both channel length and effective temperature of fast electrons are maximized here. At higher densities, the number of electrons still increases, but the temperature as well as the channel length decrease again. This is attributed to higher energy losses due to electron heating as n_e approaches n_c . Losses to ionization and ionization defocusing²⁴ occur at the channel boundaries, but play no role in the channel center, where electron trapping and acceleration takes place. It appears that this optimal plasma density is set by the laser pulse parameters since under different conditions one observes a decrease of the effective temperature with density at lower densities.¹⁹

3. Angular dependence

The emittance of electron beam emerging from the plasma channel has been studied using the setup shown in Fig. 7. By keeping constant the distance to the focus at 14 cm and the angle subtended at $\Delta\Omega = 1$ msr, the spectrometer was rotated in the horizontal plane in steps of $\Delta\theta = 2.5^\circ$ up to a maximum angle of $\theta = 10^\circ$. In Fig. 11, the spectra for three different angles and for an electron density of 10^{20} cm^{-3} are given. The form of the off axis spectrum remains more or less Boltzmann like, but the effective temperature is strongly reduced at larger angles. The full angle at which the number of all electrons with energy greater than 1 MeV is reduced to half is found to be $\theta_{\text{FWHM}} = 13^\circ$, somewhat smaller than the value obtain from the phosphorescent screen (see Fig. 5). This divergence appears to be in agreement with the results from similar experiments at lower density and higher power obtained with a completely different method.¹⁸

Measurements at optimum electron density $n_e = 2 \times 10^{20} \text{ cm}^{-3}$ reveal that the hottest electron spectrum is

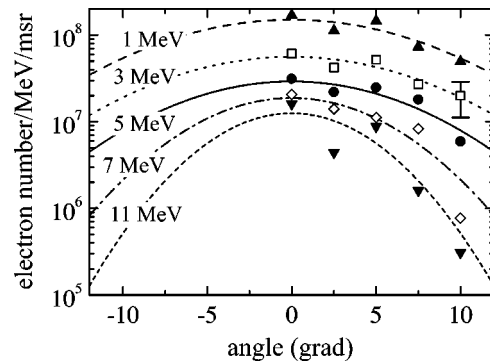


FIG. 12. Angular dependence of the electron emission within an energy bin of ± 1 MeV around the indicated energies. The experimental data (symbols) are for the optimum density $n_e = 2 \times 10^{20} \text{ cm}^{-3}$. The lines are Gaussian fits to the data.

made up of a hot component of 5 MeV in the center of the beam at 0° and colder components in the outer parts, namely 4 MeV at 5° and finally 2 MeV at 10° . This indicates that the very fast electrons with energies exceeding 10 MeV are more collimated than the less energetic ones. An analysis of all data at various angles in which the electron energy is divided into bins of ± 1 MeV illustrates this behavior and is given in Fig. 12. Here, the angular spread of electrons in five different energy ranges is shown. It diminishes from 16.5° FWHM for 1-MeV-electrons to 9° for 11-MeV-electrons. Similar measurements in the perpendicular direction show that, within the accuracy of the measurements, the electron beam is azimuthally symmetric. This confirms the result obtained with the phosphorescent screen and shown in Fig. 5.

The angle integrated spectra for various densities are shown in Fig. 13. They represent the electron distribution within a cone with angle of 20° corresponding to a solid angle of 100 msr. Here similar tendency is observed as in the on-axis spectra of Fig. 9. The effective temperature increases with the density to a maximum of 3.3 MeV and then drops for higher densities. Since the outer parts of the beam are somewhat “colder,” the angle averaged temperatures are generally lower.

The total number of all electrons emitted with energy $E > 1$ MeV inside the 20° cone along the laser axis is given

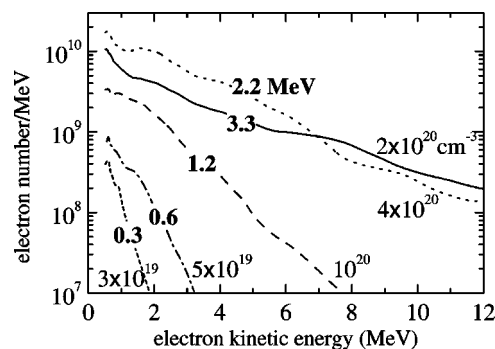


FIG. 13. Dependence of the electron-spectrum integrated over $\Delta\Omega = 100$ msr solid angle on different electron densities (labeled by normal letters). Bold letters give the effective temperatures of the (not shown) exponential fits.

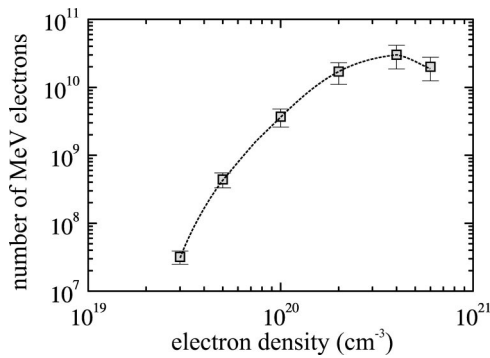


FIG. 14. Variation with the electron density of the total number of electrons with energy > 1 MeV. Symbols are experimental points and dotted line a fit.

in Fig. 14 as a function of electron density. It is seen that the number of fast electrons increases sharply with density in accordance with the results in Fig. 10 and once more confirming that efficient acceleration is only possible when $P_L > P_c$. Although it exhibits a saturation tendency at high densities, the fast electron number increases further beyond the optimum density of $2 \times 10^{20} \text{ cm}^{-3}$ to a maximum value of 3×10^{10} -MeV electrons. This corresponds to a laser-energy-to-MeV-electron efficiency of 5%. Assuming that the emission of electron lasts for ≈ 300 fs then the corresponding current is of the order of ~ 10 kA. The duration of electron emission is estimated as the sum of the laser pulse duration and of the time difference between a 10-MeV electron and an 1-MeV electron to travel the length of the channel. It is interesting to note that the beam current at laser power of 50 TW, but with longer laser pulses was estimated to be only by a factor of 6 higher.¹⁸ The electron beam current is reasonably close to the Alfvén limit, which for 5-MeV electrons is 180 kA indicating that propagation might be affected by self-generated magnetic fields.

4. Intensity dependence

The scaling of the effective electron temperature and of the total number of MeV electrons with the focal laser intensity is an important piece of information for two reasons: (a) It can provide insight and help in the identification of the dominant electron acceleration mechanism and (b) for application purposes of the relativistic electron beam where a large number of MeV electrons are required (see Sec. IV). In the investigations we have performed, the focal intensity was varied in two different ways. First, while keeping the pulse duration constant the energy was reduced by varying the delay between seed pulse and pump laser pulse in the multipass amplifier of the ATLAS laser system. In the second method the energy was kept constant, but the pulse duration was varied by changing the grating distance in the pulse compressor. In both cases, the pulse duration and energy output was monitored using accordingly a single shot autocorrelator and a calorimeter. For each intensity value, the electron spectrum was measured in absolute numbers and two quantities were thus deduced; the effective temperature T_{eff} and the total number of MeV electrons N_e .

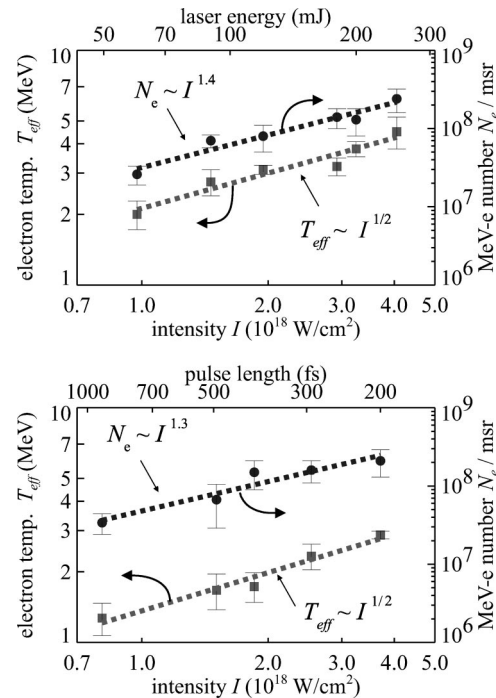


FIG. 15. Scaling of the effective electron temperature (squares) and total number of MeV electrons (circles) with intensity. Top: variation of the intensity with the laser pulse energy. Bottom: variation of the intensity with the laser pulse duration. In both cases, the $T_{\text{eff}} \propto I^{1/2}$ and the $N_e \propto I^{3/2}$ fits to the data are shown by the dashed lines.

The dependence of the effective temperature and of the total number of MeV electrons on vacuum focus intensity is shown for both cases in Fig. 15. The electron density was kept at its optimum value of $2 \times 10^{20} \text{ cm}^{-3}$ and the intensity was reduced from its maximum value by a factor of 5 at most so that even for the lowest intensity the self-focusing condition $P_L > P_{\text{RSF}}$ was satisfied. This was controlled by recording the channel length which was $250 \mu\text{m}$ for the minimum intensity. Despite the limited variation range of the intensity, the experimental results show a clear scaling with the intensity of the form $T_{\text{eff}} \propto I^{1/2} \sim a_L$ for the effective temperature and within the accuracy of the experimental data, of the form $N_e \propto I^{3/2} \sim a_L^3$ for the total number of MeV electrons. Furthermore, this scaling of T_{eff} and N_e on the intensity I appears to be independent of whether the intensity is varied via pulse width adjustment or pulse energy variation as long as a channel is created. The observed scaling for the effective temperature with the electric field of the laser has been predicted in three-dimensional PIC code simulations with an exponential density profile.³⁷ The same behavior for T_{eff} has also been observed in an experiment at higher intensities and lower densities.¹⁹

5. Gas medium dependence

The effective temperature and channel length were measured for different gases shown in Fig. 16. As can be seen, the results for hydrogen and helium are practically the same whereas for nitrogen and even more so for Ar a lower effective temperature and shorter channel length is observed. This is attributed to refraction in multi-ionized medium.²⁴ At laser

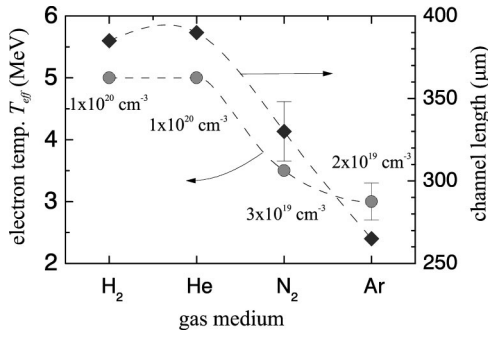


FIG. 16. Effective electron temperature and channel length observed for the indicated gas media. The corresponding atomic or molecular density is also indicated.

intensities $I_L > 10^{18}$ W/cm², hydrogen and helium are fully ionized so that the main interaction volume does not possess any density gradients and refraction has little or no effect. On the other hand, for nitrogen ionization states of 5⁺ to 7⁺ and for argon 8⁺ to 15⁺ are expected to be present. This results in strong density gradients which in turn lead to ionization induced defocusing of larger fraction of the laser pulse. The loss of energy and the lower peak intensities bring about the deterioration in the formation of the channel.

IV. PAIR CREATION AND POSITRON DETECTION

In this section, we describe an application for the laser accelerated MeV electrons in which bursts of positrons were generated. The scheme we have employed is analogous to the one used for the generation of positrons from high-Z moderators in linear electron accelerators. The electrons generated in the gas-jet target collide with a 2-mm-thick Pb slab where there is a finite probability of generating electron-positron pairs as long as the beam comprises electrons with kinetic energies ≥ 1.02 MeV. The question that arises is if the number of positrons thus produced can be unequivocally detected. There is a distinct peculiarity associated with this new source of nuclear radiation. Unlike the common sources from the decay of radioactive isotopes which emit at a given rate continuously for long period of time, this laser based source emits highly intense bursts of nuclear radiation in a very short time interval. Although this represents basically an advantage since the source can be turned “on” and “off” at will, the known coincidence techniques normally employed for the detection of nuclear radiation are not applicable in this case. Positron emission has also been reported from the direct interaction of petawatt laser pulses with solid Au targets.⁴³ However, petawatt lasers operating at high-repetition rate are not yet available and such experiments are currently restricted to large-scale facilities.

For few-MeV electrons interacting with high-Z material the most efficient processes for pair production are: (a) indirectly via Bremsstrahlung photons and (b) directly in electron nucleus collisions (the trident process).^{44,45} Assuming a converter with nuclear density N_0 , nuclear charge Z and thickness l , the probability for pair production via process (a) is

$$p_\gamma(E, E_\gamma) \approx \sigma_\gamma(E) \sigma_p(E_\gamma) N_0^2 l^2 / 2, \quad (2)$$

where σ_γ the Bremsstrahlung cross section, σ_p the γ -photon pair-production cross section, E the electron kinetic energy, and E_γ the energy of the intermediate photon. The Bremsstrahlung cross section σ_γ for electron kinetic energies $E > E_0 = 1.022$ MeV is⁴⁵

$$\sigma_\gamma \approx 11Z^2 \left[0.83 \left(\frac{E_0}{E} - 1 \right) - \ln \frac{E_0}{E} \right] \text{mb}. \quad (3)$$

For $E \sim 3$ MeV, Eq. (3) yields $\sigma_\gamma \sim 6Z^2$ mb. The cross section for the generation of an electron-positron pair via the Bremsstrahlung photons increases linearly for photon energies $E_\gamma < 5$ MeV but only as $\sim \ln E_\gamma$ for higher energies. Taking into account the values given in Ref. 46 for the appropriate energy range, we have calculated $\sigma_p(E_\gamma)$ and used it in Eq. (2). In the energy range of interest $\sigma_p \approx Z^2$ mb.

Similarly, the probability for the trident process to occur is

$$p_t(E) \approx \sigma_t(E) N_0 l \quad (4)$$

with σ_t the trident pair-production cross section. The dependence of σ_t on the electron energy E exhibits a strong increase for $E < 6$ MeV according to the expression,⁴⁴

$$\sigma_t \approx 5 \times 10^{-6} Z^2 (\gamma - 3)^{3.6} \text{mb for } \gamma < 13, \quad (5)$$

whereas for higher energies the increase is moderate:⁴⁷

$$\sigma_t \approx 1.6 \times 10^{-3} Z^2 (\ln \gamma)^3 \text{mb for } \gamma > 13. \quad (6)$$

The relativistic factor γ corresponding to the electron kinetic energy E is $\gamma = (E + mc^2)/mc^2$.

In using Eqs. (2), (4), it has been assumed that $l \ll R_e, \mu^{-1}$, where R_e the electron range and μ the absorption coefficient for γ 's in the converter material. As all cross sections have a Z^2 dependence on the nuclear charge Z ,⁴⁴⁻⁴⁷ the indirect process scales as $Z^4 (N_0 l)^2$ while the direct is linear with $Z^2 N_0 l$. Therefore, for a given electron energy E high-Z material and thick converter favor the indirect process.

An estimate of the fraction of primary electrons converted into positrons N_{e^+}/N_{e^-} as a function of the electron primary energy can be obtained if one assumes $E_\gamma \approx E/2 + m_e c^2$ for the energy of those γ -photons appropriate for pair production.⁴⁵ For a $l = 2$ mm thick lead converter with $N_0 = 3.3 \times 10^{22}$ cm⁻³, using the expressions for the cross sections given in Eqs. (2)–(6) one finds the results depicted in Fig. 17. It is seen that (i) in the electron energy range of $E < 15$ MeV, the indirect process is dominant and (ii) for 3 MeV electrons, a fraction of 10^{-3} will be converted into positrons.

While this method of pair production is straight forward, detection of the positrons is difficult. As already mentioned, the standard method of detecting 512-keV annihilation photons (e.g., with coincidence counters) is precluded due to the intense burst of MeV photons which makes the detection of single photon particularly impossible. Therefore, a more direct way was chosen here and it is schematically depicted in Fig. 18. It uses a single thick scintillator that had to be carefully shielded to suppress the background signal due to stray γ 's to a minimum on account of the weak positron signal. To

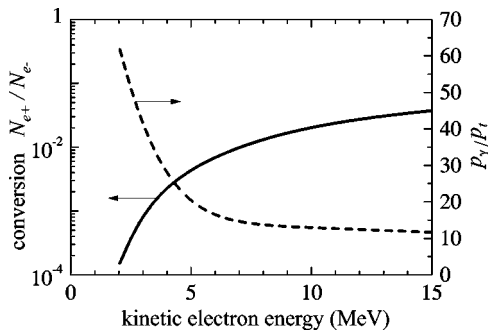


FIG. 17. Variation of the electron to positron conversion efficiency for a 2-mm-thick Pb converter (solid line) and of the probability ratio of indirect to direct process (dashed line) as a function of the primary electron energy.

this effect, the separation of the positrons from the primary electrons emanating from the converter by a magnetic field and the heavy shielding with lead bricks of the scintillator detector were crucial to the detection of the positrons. The primary electrons were collimated in a plastic block with a 1-cm-diameter hole. The low-Z material stops electrons without producing undue Bremsstrahlung. The converter was a 2-mm-thick lead disk positioned inside the collimator (see Fig. 18) at a distance of 16 cm from the gas-jet where the laser beam was focused. The collimation of the beam results in reducing the number of MeV electrons to $(8 \pm 1.7) \times 10^8$ (from a total of 2×10^{10}) for performing a clean demonstration experiment. The positrons emanating from the converter have a quasi-isotropic distribution.⁴⁶ Those traveling in the laser direction are collimated by another 2 cm in the plastic collimator before they enter the region where a magnetic field of $B \approx 1.50$ kG from two permanent magnets is present. Due to the magnetic field, positrons describe a 180° orbit and are detected by a light tight, 1.5-cm-thick plastic scintillator coupled to a photomultiplier tube. The absolutely calibrated detector covers the positron energy range of $\Delta E = 2 \pm 0.08$ MeV and subtends a solid angle of $\Delta\Omega_{e^+} = 7$ msr to the converter.

The electron energy distribution was carefully characterized at the beginning of the experiment with the help of the multi-channel electron spectrometer¹⁰ and its reproducibility was established. The spectrum is given in Fig. 19 and it can be fitted to a Boltzmann distribution with an effective tem-

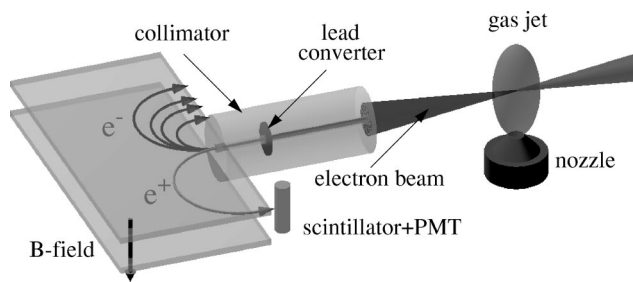


FIG. 18. Schematic of the miniaturized arrangement used for the production of positrons. The MeV electrons produced in the gas jet are collimated and converted into γ 's and pairs in the 2-mm-thick Pb converter. The positrons are separated from the primary and secondary electrons via a static magnetic field and detected by the thick scintillator. Not shown is the heavy lead brick shielding used to reduce the signal background due to the generated γ 's.

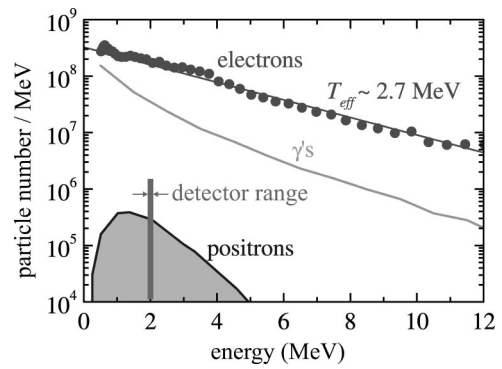


FIG. 19. Measured energy distribution of the primary electrons (full circles, exponential fit as dashed line) used to produce positrons. The calculated spectrum of the generated γ 's and the expected positron spectrum is also shown. The calculation assumes a 2-mm-thick Pb converter and is based on the cross-sections given in Eqs. (2)–(6). The stripe denotes the energy range covered by the detector. It encompasses $\sim 5\%$ of the total number of positrons.

perature of $T_{\text{eff}} = 2.7 \pm 0.1$ MeV. It should be noted here that during this experimental series, the laser system characteristics had changed slightly compare to those described in Sec. III and under which the electron acceleration measurements were performed. This had as a consequence a lower effective electron temperature. The feasibility of the positron detection was checked as follows: For the measured electron distribution and for the converter employed, the energy distribution of the γ -photons was calculated using the cross section in Eq. (3). This is illustrated in Fig. 19. Moreover, assuming that the positron-electron pair shares the energy of the γ -photon or primary electron, Eqs. (2) and (4) give an estimate of the expected positron spectrum due to both processes. As is shown in Fig. 19, it peaks in the energy range of 1–2 MeV and drops rapidly at higher energies. The latter is due to the converter thickness that becomes more transmissive for the high energy γ 's and electrons. The number of positrons generated N_{e^+} per laser shot can be estimated now based on the value $\Delta N_{e^+} / \Delta E \approx 3 \times 10^5 e^+ / \text{MeV}$ obtained from the spectrum in Fig. 19 for 2 MeV positrons as follows: $N_{e^+} \approx (\Delta N_{e^+} / \Delta E) (\Delta\Omega_{e^+} / 4\pi) \Delta E \sim 27 e^+ / \text{shot}$.

Indeed, the measurements confirmed the presence of 30 ± 15 positrons per shot. It should be mentioned here that despite the careful shielding of the detector, the signal due to the energy deposited by the 30 positrons per pulse amounts to only 6% of the background signal. This difficulty was circumvented by performing a difference measurement, i.e., with and without positrons and statistically analyzing the results over a large number of shots. A detailed description of the experimental procedure and analysis is given in Ref. 10. In order to further substantiate our experimental result, we have performed detailed Monte Carlo-type simulations using the code GEANT.⁴⁸ This code allows the user to exactly simulate the experimental setup, i.e., collimator, converter, shielding, magnet, vacuum chamber wall, and detector. Two systematic variations were undertaken. At first for a fixed electron temperature of $T_{\text{eff}} = 3$ MeV, the converter thickness was varied leading to an optimum $l_{\text{opt}} = 2$ mm. Second, for fixed converter thickness l_{opt} , the primary electron tempera-

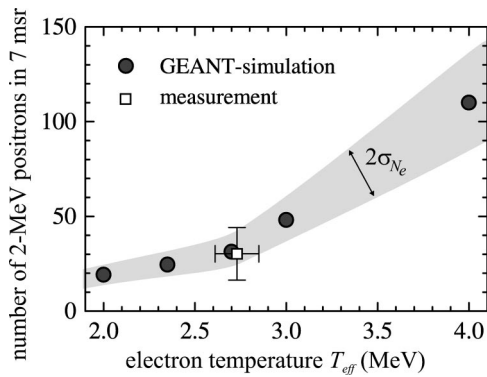


FIG. 20. Number of positrons seen by the detector as a function of the effective electron temperature: (i) GEANT simulation (circles), (ii) measurement (square). The shaded area indicates the uncertainty σ_{N_e} associated with the fluctuation in the total number of measured electrons.

ture was varied between $T_{\text{eff}}=2\text{--}5$ MeV. The simulations results for selected electron temperatures along with the experimental value for $T_{\text{eff}}=2.7\pm 0.1$ MeV are presented in Fig. 20 where the number of positrons expected within the 2 ± 0.08 MeV channel is given. As can be seen, the simulations predict the experimentally measured number of positrons for the geometry used.

Scaling the number of positrons detected within 0.16 MeV energy range and 7.0 msr solid angle to full energy spread (see Fig. 19) and solid angle, one obtains a total number of 10^6 positrons per laser pulse. Using the full uncollimated electron beam gives a positron number of $\sim 2\times 10^7$ per laser pulse, which for 10 Hz operation corresponds to an activity of 2×10^8 Bq. These values pertain to the ATLAS laser system which for the experiments presented here was delivering $P_L\sim 1.2$ TW per pulse producing a maximum $T_{\text{eff}}\approx 5$ MeV. However, table-top laser systems with power output of $P_L> 15$ TW are already reality. In this case according to the scaling law $T_{\text{eff}}\propto I^{1/2}$ given in Fig. 15, one would expect an electron temperature of $T_{\text{eff}}\sim 17$ MeV. Then, at these higher attainable laser intensities the increase in the T_{eff}

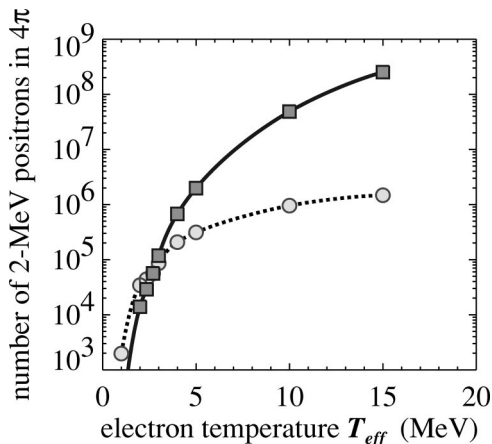


FIG. 21. GEANT simulation for the number of 2 ± 0.1 MeV positrons produced in 4π as a function of the effective electron temperature for a 2-mm-thick Pb converter. For constant number of MeV electrons $N_e=\text{const}$ (circles and dotted line) and for $N_e\propto I^{3/2}$ (squares and solid line).

of the primary electrons leads to a sharp rise of the positron output. This is depicted in Fig. 21 where the predictions of the GEANT code for constant number of MeV electrons N_e and the same type of converter as in the experiment are given. If one takes into consideration that the number of MeV electrons also increases with the intensity according to the scaling $N_e\propto I^{3/2}\propto T_{\text{eff}}^3$ (see Fig. 15), the positron output is expected to increase nearly three orders of magnitude for $T_{\text{eff}}\sim 15$ MeV. These estimates assume that the scaling laws of Fig. 15 continue to be valid for higher intensities. As can be seen from Fig. 21, the positron yield for a given converter thickness and for $N_e=\text{constant}$ exhibits a saturation for higher T_{eff} values. This is attributed to the larger range in the converter material of the more energetic electrons and generated γ 's. Indeed, for $T_{\text{eff}}\sim 15$ MeV and twice as thick lead converter a factor of 2 increase in the positron yield is observed. Therefore, by optimizing the converter thickness for a given electron temperature, one can expect even higher yields approaching equivalent activities of $> 10^{11}$ Bq.

V. DISCUSSION

In the interaction of ultra-high-intensity pulses with solid targets the fast electron distribution is characterized by an effective temperature given by the quiver energy of that electron in the laser field, i.e., $E_{\text{osc}}=(\gamma_{\text{osc}}-1)m_e c^2$ with $\gamma_{\text{osc}}=\sqrt{1+a_L^2}$.⁴⁹ For laser intensities in the range of $10^{18}\text{--}10^{19}$ W/cm², the corresponding effective temperature is $T_{\text{eff}}\approx 0.2\text{--}1$ MeV. However, experiments with gas jet targets consistently produce a fast electron spectrum with a considerably higher effective temperature, from a few MeV to over 10 MeV.^{9,15-19,33,34} Moreover, it was experimentally found that about 5% of the laser energy appears in the form of a beam of collimated relativistic electrons.⁹ It is apparent that an acceleration mechanism due to collective effects is responsible for this rather efficient laser energy transfer to plasma electrons. Two mechanisms, i.e., the Laser Wakefield Acceleration (LWFA) and the Direct Laser Acceleration (DLA) have been outlined in Sec. II B.

Given the potential applications envisaged for these electrons,^{12,35} the interest is high in discerning under which conditions a particular mechanism is dominant. Unfortunately, no ‘‘footprint’’ which is uniquely associated with a particular acceleration mechanism and which can be experimentally verified has been yet found. The claims over dominance of one or the other acceleration mechanism are made on the basis of detailed comparison with relativistic PIC codes.^{9,19}

In this context, we have also performed a detailed comparison with a full-scale three-dimensional PIC simulation code⁵⁰ the detailed results of which have been reported elsewhere.⁹ The three-dimensional capability of this code allows the treatment of the experimental geometry in a realistic way and it uses as input the experimental profiles for the laser pulse and gas target density. For the optimal experimental parameters, i.e., $n_e=2\times 10^{20}$ cm⁻³, corresponding to electrons generated with highest energy, the three-dimensional PIC simulations reproduce the experimental measurements reliably not only qualitatively but also in the

absolute number of accelerated electrons in a given energy range and solid angle cone.⁹ A more detailed analysis of the electron dynamics as obtained from the code output⁹ shows that for the parameters of our experiment (high density, laser pulse larger than plasma wavelength) the laser wakefield exists only for short time at the leading edge of the laser pulse. Furthermore, it is found that most of the electron energy gain is due to the transverse laser electric field with the laser magnetic field converting the transverse momentum into longitudinal one.^{37,38}

More recently, a similar analysis has been performed for the experiment described in Ref. 19, which in contrast to our results indicates that most of the fast electrons are produced via longitudinal acceleration due to the plasma wakefield. Furthermore, it was found that the maximum energy acquired by the electrons varies with density as $\gamma_{\max} \sim \omega_L^2/\omega_p^2 \sim 1/n_e$ as one would expect from the LWFA mechanism.³⁵ This behavior is opposite to our experimental finding in which the effective electron temperature increases with density up to a maximum value of $T_{\text{eff}}=5$ keV for $n_e=2 \times 10^{20} \text{ cm}^{-3}$ (see Fig. 10). The main difference between the two investigations is that ours was performed in a previously unexplored regime, characterized by fs-laser pulses of relatively *low-intensity* ($<6 \times 10^{18} \text{ W/cm}^2$) interacting with a *high-density* ($n_e \sim 0.05n_c - 0.3n_c$) gas jet, whereas the results as given in Ref. 19 pertain to *high-intensity* laser pulses ($2 \times 10^{19} \text{ W/cm}^2$) and *low-density* ($n_e \sim 0.005n_c - 0.05n_c$) gas jet. Although other factors like focal spot or gas-jet density profile (large gradient vs uniform profile) might play a role, the results from these two experiments and their analysis suggest that the laser pulse duration (200 fs vs 35 fs) and the density regime ($\sim 2 \times 10^{20} \text{ cm}^{-3}$ vs $\sim 3 \times 10^{19} \text{ cm}^{-3}$) are decisive in determining which mechanism is dominant. Indeed, both experiments were performed in the SM-LWFA regime, i.e., in a parameter range where $\tau_L \omega_p/\pi > 1$. However, for our parameters due to higher density and longer pulse duration $\tau_L \omega_p/\pi \approx 50$, while for those of Ref. 19 $\tau_L \omega_p/\pi \approx 4$. Furthermore, three-dimensional PIC simulation results have revealed that in this regime of high density and long laser pulse duration, the DLA mechanism overtakes the SM-LWFA if self-channeling occurs trapping laser power $P \gg P_{\text{RSF}}$.⁵¹ It appears that the formation of a robust channel is a prerequisite for the DLA mechanism to dominate over the SM-LWFA. This could be the main reason for the discrepancy between the two experiments since for the short laser pulses used in Ref. 19 might not have been enough time for the channel to fully develop and establish the quasi-static fields necessary for the DLA mechanism to become effective.^{37,38}

In recent years positrons have played an important role in applications in diverse fields of physics, e.g., surface physics,⁵² positronium spectroscopy⁵³ and electron-positron plasmas.⁵⁴ Although for most of these applications conventional radioactive sources like ^{22}Na or ^{58}Co are currently used, the distinct possibility exists to replace them with laser driven positron sources. The potential to create large number of e^-e^+ pairs using ultra-intense lasers has been considered in estimates¹⁴ and theoretical investigations,⁵⁵ however, the

results presented in Ref. 10 and here demonstrate that a 10 Hz laser driven positron source is indeed realizable. Given the prodigious technological advances in laser technology,⁵⁶ it is almost certain that in the near future there will be laser systems delivering pulsed power of 100 TW or more at repetition rates of 1 kHz. The fluxes of positrons that can be generated by such lasers would then be comparable to those from electron linear accelerators using a facility that can fit in a normal size room. Other obvious advantages of laser driven positron sources is the fact that they can be turned off when they are not needed thus reducing considerably the radiation hazards associated with radioactive sources. The pulsed character of the source with the immense peak intensities, can be exploited in positron-annihilation spectroscopy to simplify the cumbersome timing electronics since the start signal is well defined by the laser pulse. It is beyond doubt that the unique properties of this pulsed positron source will be of advantage to other applications as well.

ACKNOWLEDGMENTS

The authors would like to express their appreciation to A. Pukhov and J. Meyer-ter-Vehn for fruitful discussions and for reading the manuscript and making useful suggestions. The technical assistance of H. Haas, A. Böswald and P. Sachsenmaier is greatly appreciated.

This research was supported by the Commission of the EC within the framework of the Association Euratom—Max-Planck-Institut für Plasmaphysik and DFG Contract No. Ha 1101/7-1.

¹G. A. Mourou, C. P. J. Barty, and M. D. Perry, Phys. Today **51** (1), 22 (1998).

²J. D. Kmetec, C. L. Gordon III, J. J. Macklin, B. E. Lemoff, G. S. Brown, and S. E. Harris, Phys. Rev. Lett. **68**, 1527 (1992).

³C. Gahn, G. Pretzler, A. Saemann, G. D. Tsakiris, K. J. Witte, D. Gas-smann, T. Schätz, U. Schramm, P. Thirolf, and D. Habs, Appl. Phys. Lett. **73**, 3662 (1998).

⁴S. Kohlweyer, G. D. Tsakiris, C.-G. Wahlström, C. Tillman, and I. Mercer, Opt. Commun. **177**, 431 (1995).

⁵D. von der Linde, T. Engers, G. Jenke, P. Agostini, G. Grillon, E. Nibbering, A. Mysyrowicz, and A. Antonetti, Phys. Rev. A **52**, R25 (1995).

⁶M. Zepf, G. D. Tsakiris, G. Pretzler, I. Watts, D. M. Chambers, P. A. Norreys, U. Andiel, A. E. Dangor, K. Eidmann, C. Gahn, A. Machacek, J. S. Wark, and K. Witte, Phys. Rev. E **58**, R5253 (1998).

⁷G. Pretzler, A. Saemann, A. Pukhov, D. Rudolph, T. Schätz, U. Schramm, P. Thirolf, D. Habs, K. Eidmann, G. D. Tsakiris, J. Meyer-ter-Vehn, and K. J. Witte, Phys. Rev. E **58**, 1165 (1998).

⁸T. Ditmire, J. Zweiback, V. P. Yanovsky, T. E. Cowan, G. Hays, and K. B. Wharton, Nature (London) **398**, 489 (1999).

⁹C. Gahn, G. D. Tsakiris, A. Pukhov, J. Meyer-ter-Vehn, G. Pretzler, P. Thirolf, D. Habs, and K. J. Witte, Phys. Rev. Lett. **83**, 4772 (1999).

¹⁰C. Gahn, G. D. Tsakiris, G. Pretzler, K. J. Witte, C. Delfin, C.-G. Wahlström, and D. Habs, Appl. Phys. Lett. **77**, 2662 (2000).

¹¹E. Esarey, P. Sprangle, J. Krall, and A. Ting, IEEE Trans. Plasma Sci. **24**, 252 (1996).

¹²M. Tabak, J. Hammer, M. E. Glinsky, W. L. Kruer, S. C. Wilks, J. Woodworth, E. M. Campbell, M. D. Perry, and R. J. Mason, Phys. Plasmas **1**, 1626 (1994).

¹³P. L. Shkolnikov, A. E. Kaplan, A. Pukhov, and J. Meyer-ter-Vehn, Appl. Phys. Lett. **71**, 3471 (1997).

¹⁴S. Karsch, D. Habs, T. Schätz, U. Schramm, P. G. Thirolf, J. Meyer-ter-Vehn, and A. Pukhov, Laser Part. Beams **17**, 565 (1999).

¹⁵C. I. Moore, A. Ting, K. Krushelnick, E. Esarey, R. F. Hubbard, B. Hafizi, H. R. Burris, C. Manka, and P. Sprangle, Phys. Rev. Lett. **79**, 3909 (1997).

¹⁶R. Wagner, S.-Y. Chen, A. Maksimchuk, and D. Umstadter, Phys. Rev. Lett. **78**, 3125 (1997).

¹⁷D. Gordon, K. C. Tzeng, C. E. Clayton, A. E. Dangor, V. Malka, K. A.

- Marsh, A. Modena, W. B. Mori, P. Muggli, Z. Najmudin, D. Neely, C. Danson, and C. Joshi, *Phys. Rev. Lett.* **80**, 2133 (1998).
- ¹⁸M. I. K. Santala, Z. Najmudin, E. L. Clark, M. Tatarakis, K. Krushelnick, A. E. Dangor, V. Malka, J. Faure, R. Allott, and R. J. Clarke, *Phys. Rev. Lett.* **86**, 1227 (2001).
- ¹⁹V. Malka, J. Faure, J. R. Marquès, F. Amiranoff, J. P. Rousseau, S. Ranc, J. P. Chambaret, Z. Najmudin, B. Walton, P. Mora, and A. Solodov, *Phys. Plasmas* **8**, 2605 (2001).
- ²⁰C. E. Max, J. Arons, and A. B. Langdon, *Phys. Rev. Lett.* **33**, 209 (1974).
- ²¹P. Sprangle, E. Esarey, and A. Ting, *Phys. Rev. A* **41**, 4463 (1990).
- ²²P. Sprangle, E. Esarey, and A. Ting, *Phys. Rev. Lett.* **64**, 2011 (1990).
- ²³P. Sprangle, E. Esarey, and J. Krall, *Phys. Plasmas* **3**, 2183 (1996).
- ²⁴R. Fedosejevs, X. F. Wang, and G. D. Tsakiris, *Phys. Rev. E* **56**, 4615 (1997).
- ²⁵G.-Z. Sun, E. Ott, Y. C. Lee, and P. Guzdar, *Phys. Fluids* **30**, 526 (1987).
- ²⁶P. Sprangle, C. M. Tang, and E. Esarey, *IEEE Trans. Plasma Sci.* **15**, 145 (1987).
- ²⁷J. C. Solem, T. S. Luk, K. Boyer, and C. K. Rhodes, *IEEE J. Quantum Electron.* **25**, 2423 (1989).
- ²⁸A. B. Borisov, A. V. Borovskiy, O. B. Shiryayev, V. V. Korobkin, A. M. Prokhorov, J. C. Solem, T. S. Luk, K. Boyer, and C. K. Rhodes, *Phys. Rev. A* **45**, 5830 (1992).
- ²⁹A. B. Borisov, O. B. Shiryayev, A. McPherson, K. Boyer, and C. K. Rhodes, *Plasma Phys. Controlled Fusion* **37**, 569 (1995).
- ³⁰X. Wang, M. Krishnan, N. Saleh, H. Wang, and D. Umstadter, *Phys. Rev. Lett.* **84**, 5324 (2000).
- ³¹A. Pukhov and J. Meyer-ter-Vehn, *Phys. Rev. Lett.* **76**, 3975 (1996); *Phys. Plasmas* **5**, 1880 (1998).
- ³²M. Borghesi, A. J. McKinnon, L. Barringer, R. Gaillard, L. A. Gizzi, C. Meyer, and O. Willi, *Phys. Rev. Lett.* **78**, 879 (1997).
- ³³A. Modena, Z. Najmudin, A. E. Dangor, C. E. Clayton, K. A. Marsh, C. Joshi, V. Malka, C. B. Darrow, C. Danson, D. Neely, and F. N. Walsh, *Nature (London)* **377**, 606 (1995).
- ³⁴D. Umstadter, S.-Y. Chen, A. Maksimchuk, G. Mourou, and R. Wagner, *Science* **273**, 472 (1996).
- ³⁵T. Tajima and J. M. Dawson, *Phys. Rev. Lett.* **43**, 267 (1979).
- ³⁶D. Umstadter, E. Esarey, and J. Kim, *Phys. Rev. Lett.* **72**, 1224 (1994).
- ³⁷A. Pukhov, Z.-M. Sheng, and J. Meyer-ter-Vehn, *Phys. Plasmas* **6**, 2847 (1999).
- ³⁸G. D. Tsakiris, C. Gahn, and V. K. Tripathi, *Phys. Plasmas* **7**, 3017 (2000).
- ³⁹E. D. Courant, C. Pellegrini, and W. Zakowicz, *Phys. Rev. A* **32**, 2813 (1985).
- ⁴⁰M. Borghesi, A. J. Mackinnon, R. Gaillard, O. Willi, A. Pukhov, and J. Meyer-ter-Vehn, *Phys. Rev. Lett.* **80**, 5137 (1998).
- ⁴¹Y. M. Li and R. Fedosejevs, *Meas. Sci. Technol.* **5**, 1197 (1994).
- ⁴²C. Gahn, G. D. Tsakiris, K. J. Witte, P. Thirolf, and D. Habs, *Rev. Sci. Instrum.* **71**, 1642 (2000).
- ⁴³T. E. Cowan, M. D. Perry, M. H. Key, T. R. Ditmire, S. P. Hatchett, E. A. Henry, J. D. Moody, M. J. Moran, D. M. Pennington, T. W. Phillips, T. C. Sangster, J. A. Sefcik, M. S. Singh, R. A. Snavely, M. A. Stoyer, S. C. Wilks, P. E. Young, Y. Takahashi, B. Dong, W. Fountain, T. Parnell, J. Johnson, A. W. Hunt, and T. Kühl, *Laser Part. Beams* **17**, 773 (1999).
- ⁴⁴J. W. Shearer, J. Garrison, J. Wong, and J. E. Swain, *Phys. Rev. A* **8**, 1582 (1973).
- ⁴⁵P. L. Shkolnikov and A. E. Kaplan, *J. Nonlinear Opt. Phys. Mater.* **6**, 161 (1997).
- ⁴⁶R. B. Evans, *The Atomic Nucleus* (McGraw-Hill, New York, 1995), pp. 701–710.
- ⁴⁷W. Heitler, *The Quantum Theory of Radiation* (Clarendon, Oxford, 1954), pp. 256–268.
- ⁴⁸R. Brun *et al.*, GEANT Users's Guide, CERN report DD/EE/82 (1982), unpublished.
- ⁴⁹G. Malka and J. L. Miquel, *Phys. Rev. Lett.* **77**, 75 (1996).
- ⁵⁰A. Pukhov, *J. Plasma Phys.* **61**, 425 (1999).
- ⁵¹A. Pukhov, private communications (2001).
- ⁵²C. Szeles and K. G. Lynn, in *Encyclopedia of Applied Physics*, edited by G. L. Trigg (VCH, New York, 1996), Vol. 14, pp. 607–632.
- ⁵³A. Rich, *Rev. Mod. Phys.* **53**, 127 (1981).
- ⁵⁴R. G. Greaves and C. M. Surko, *Phys. Plasmas* **4**, 1528 (1997).
- ⁵⁵E. P. Liang, S. C. Wilks, and M. Tabak, *Phys. Rev. Lett.* **81**, 4887 (1998).
- ⁵⁶S. Sartania, Z. Cheng, M. Lenzner, G. Tempea, Ch. Spielmann, and F. Krausz, *Opt. Lett.* **22**, 1562 (1997).